PHYSICAL REVIEW LETTERS

Characterization of a Two-Transmon Processor with Individual Single-Shot Qubit Readout

A. Dewes,[1] F. R. Ong,[1] V. Schmitt,[1] R. Lauro,[1] N. Boulant,[2] P. Bertet,[1] D. Vion,[1] and D. Esteve[1]

[1]*Quantronics group, Service de Physique de l'État Condensé (CNRS URA 2464), IRAMIS, DSM, CEA-Saclay,
91191 Gif-sur-Yvette, France*
[2]*LRMN, Neurospin, I2BM, DSV, 91191CEA-Saclay, 91191 Gif-sur-Yvette, France*
(Received 26 September 2011; published 2 February 2012)

We report the characterization of a two-qubit processor implemented with two capacitively coupled tunable superconducting qubits of the transmon type, each qubit having its own nondestructive single-shot readout. The fixed capacitive coupling yields the $\sqrt{i\mathrm{SWAP}}$ two-qubit gate for a suitable interaction time. We reconstruct by state tomography the coherent dynamics of the two-bit register as a function of the interaction time, observe a violation of the Bell inequality by 22 standard deviations after correcting readout errors, and measure by quantum process tomography a gate fidelity of 90%.

Quantum-information processing is one of the most appealing ideas for exploiting the resources of quantum physics and performing tasks beyond the reach of classical machines [1]. Ideally, a quantum processor consists of an ensemble of highly coherent two-level systems, the qubits, that can be efficiently reset, that can follow any unitary evolution needed by an algorithm using a universal set of single- and two-qubit gates, and that can be readout projectively. In the domain of electrical quantum circuits [2], important progress [3–7] has been achieved recently with the operation of elementary quantum processors based on different superconducting qubits. Those based on transmon qubits [3,4,8,9] are well protected against decoherence but embed all the qubits in a single resonator used both for coupling them and for joint readout. Consequently, individual readout of the qubits is not possible and the results of a calculation, as the Grover search algorithm demonstrated on two qubits [3], cannot be obtained by running the algorithm only once. Furthermore, the overhead for getting a result from such a processor without single-shot readout but with a larger number of qubits overcomes the speed-up gain expected for any useful algorithm. The situation is different for processors based on phase qubits [5,6,10], where the qubits are more sensitive to decoherence but can be read individually with high fidelity, although destructively. This significant departure from the wished scheme can be circumvented, when needed, since a destructive readout can be transformed into a nondestructive one at the cost of adding one ancilla qubit and one extra two-qubit gate for each qubit to be read projectively. Moreover, energy release during a destructive readout can result in a sizable cross talk between the readout outcomes, which can also be solved at the expense of a more complex architecture [10,11].

In this work, we operate a new architecture that comes closer to the ideal quantum processor design than the above-mentioned ones. Our circuit is based on frequency tunable transmons that are capacitively coupled. Although the coupling is fixed, the interaction is effective only when the qubits are on resonance, which yields the $\sqrt{i\mathrm{SWAP}}$ universal gate for an adequate coupling duration. Each qubit is equipped with its own nondestructive single-shot readout [12,13] and the two qubits can be read with low cross talk. In order to characterize the circuit operation, we reconstruct the time evolution of the two-qubit register density matrix during the resonant and coherent exchange of a single quantum of excitation between the qubits by quantum state tomography. Then, we prepare a Bell state with concurrence 0.85, measure the Clauser-Horne-Shimony-Holt (CHSH) entanglement witness, and find a violation of the corresponding Bell inequality by 22 standard deviations. We then characterize the $\sqrt{i\mathrm{SWAP}}$ universal gate operation by determining its process map with quantum process tomography [1]. We find a gate fidelity of 90% due to qubit decoherence and systematic unitary errors.

The circuit implemented is schematized in Fig. 1(a): the coupled qubits with their respective control and readout subcircuits are fabricated on a Si chip [see Supplemental Material (SM), Sec. I [14]]. The chip is cooled down to 20 mK in a dilution refrigerator and connected to room-temperature sources and measurement devices by attenuated and filtered control lines and by two measurement lines equipped with cryogenic amplifiers. Each transmon $j =$ I, II is a capacitively shunted SQUID characterized by its Coulomb energy E_C^j for a Cooper pair, the asymmetry d_j between its two Josephson junctions, and its total effective Josephson energy $E_J^j(\phi_j) = E_J^j |\cos(x_j)| \sqrt{1 + d_j^2 \tan^2(x_j)}$, with $x_j = \pi \phi_j / \phi_0$, ϕ_0 the flux quantum, and ϕ_j the magnetic flux through the SQUIDs induced by two local current lines with a 0.5 GHz bandwidth. The transition frequencies $\nu_j \simeq \sqrt{2 E_C^j E_J^j}/h$ between the two lowest energy states $|0\rangle_j$ and $|1\rangle_j$ can thus be tuned by ϕ_j. The qubits are coupled by a capacitor with nominal value $C_c \simeq 0.13$ fF and form a register with the Hamiltonian (see Sec. II of the SM [14])
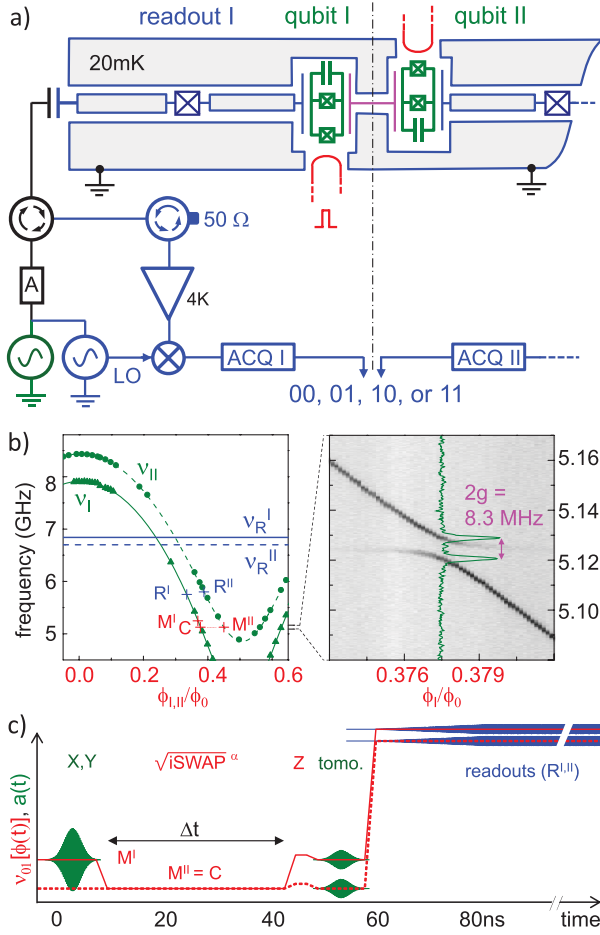
FIG. 1 (color). (a) Circuit schematics of the experiment show-ing the qubits I and II in green, their readout devices in grayed blue, and the homodyne detection circuits with their digitizer (ACQ) in blue. (b) Left-hand panel: Spectroscopy of the sample showing the resonator frequencies $\nu_R^I = 6.84$ GHz and $\nu_R^{II} = 6.70$ GHz (horizontal lines), and the measured (disks, triangles) and fitted (lines) qubit frequencies $\nu_{I,II}$ as a function of their flux bias $\phi_{I,II}$ when the other qubit is far detuned. Right-hand panel: Spectroscopic anticrossing of the two qubits revealed by the 2D plot of $p_{01} + p_{10}$ as a function of the probe frequency and of ϕ_I, at $\nu_{II} = 5.124$ GHz. (c) Typical pulse sequence including X or Y rotations, a $\sqrt{i\mathrm{SWAP}}^\alpha$ gate, Z rotations, and tomographic and readout pulses. Microwave pulses $a(t)$ for qubit (green) and for readout (blue) are drawn on top of the $\nu_{I,II}(\phi)$ dc pulses (red lines).

$H = h(-\nu_I\sigma_z^I - \nu_{II}\sigma_z^{II} + 2g\sigma_y^I\sigma_y^{II})/2$. Here h is the Planck constant, $\sigma_{x,y,z}$ are the Pauli operators, $2g = \sqrt{E_C^I E_C^{II}\nu_I\nu_{II}}/E_{Cc} \ll \nu_{I,II}$ is the coupling frequency, and E_{Cc} the Coulomb energy of a Cooper pair on the coupling capacitor. The two-qubit gate is defined in the uncoupled basis $\{|uv\rangle\} \equiv \{|0\rangle_I, |1\rangle_I\} \otimes \{|0\rangle_{II}, |1\rangle_{II}\}$, at a working point $M_{I,II}$ where the qubits are sufficiently detuned ($\nu_{II} - \nu_I \gg 2g$) to be negligibly coupled. Bringing them on resonance at a frequency ν in a time much shorter than $1/2g$ but much

longer than $1/\nu$, and keeping them on resonance during a time Δt, one implements an operation $\Theta_I\Theta_{II}\sqrt{i\mathrm{SWAP}}^{(8g\Delta t)}$, which is the product of the

$$\sqrt{i\mathrm{SWAP}} = \begin{pmatrix} 1 & 0 & 0 & 0 \\ 0 & 1/\sqrt{2} & -i/\sqrt{2} & 0 \\ 0 & -i/\sqrt{2} & 1/\sqrt{2} & 0 \\ 0 & 0 & 0 & 1 \end{pmatrix}$$

gate to an adjustable power and of two single qubit phase gates $\Theta_j = \exp(i\theta_j\sigma_z^j/2)$ accounting for the dynamical phases $\theta_j = \int 2\pi(\nu - \nu_j)dt$ accumulated during the cou-pling. The exact $\sqrt{i\mathrm{SWAP}}$ gate can thus be obtained by choosing $\Delta t = 1/8g$ and by applying a compensation rotation Θ_j^{-1} to each qubit afterward.

For readout, each qubit is capacitively coupled to its own $\lambda/2$ coplanar waveguide resonator with frequency ν_R^j and quality factor $Q_j \simeq 700$. The frequency ν_R^j is shifted by $\pm\chi$ depending on the measured qubit state, with $\chi \simeq g_0^2/(\nu_R^j - \nu_j)$ and g_0 the qubit-resonator coupling fre-quency. Each resonator is made nonlinear with a Josephson junction and is operated as a Josephson bifurca-tion amplifier, as explained in detail in [13]: ideally, it switches from a low to a high amplitude oscillating state when qubit state $|1\rangle$ is measured. Consequently, the homo-dyne measurement [see Fig. 1(a)] of two microwave pulses simultaneously applied to and reflected from the two res-onators yields a two-bit outcome uv that maps with a high fidelity the state $|uv\rangle$ on which the register is projected; the probabilities p_{uv} of the four possible outcomes are deter-mined by repeating the same experimental sequence a few 10^4 times. Single qubit rotations $u(\theta)$ by an angle θ around an axis $\vec{u}$ of the XY plane of the Bloch sphere are obtained by applying Gaussian microwave pulses directly through the readout resonators, with frequencies ν_j, phases $\varphi_j = (\vec{X}, \vec{u})$, and calibrated areas $A_j \propto \theta$; a sufficiently high power is used to compensate for the filtering effect of each resonator, which depends on the detuning $\nu_j - \nu_R^j$. Rotations around Z are obtained by changing temporarily $\nu_{I,II}$ with dc pulses on the current lines.

The sample is first characterized by spectroscopy [see Fig. 1(b)], and a fit of the transmon model to the data yields the sample parameters (see Sec. III of the SM [14]). The working points where the qubits are manipulated ($M^{I,II}$), resonantly coupled (C), and readout ($R^{I,II}$) are chosen to yield sufficiently long relaxation times ~ 0.5 μs [15] dur-ing gates, negligible residual coupling during single qubit rotations and readout, and best possible fidelities at read-out. Figure 1(b) shows these points as well as the spectro-scopic anticrossing of the two qubits at point C, where $2g = 8.3$ MHz in agreement with the design value of C_c. Then, readout errors are characterized at $R^{I,II}$ (see Sec. IV of the SM [14]): In a first approximation, the errors are independent for the two readouts and are of about 10% and 20% when reading $|0\rangle$ and $|1\rangle$, respectively. This limited

fidelity results for a large part from energy relaxation of the qubits at readout. In addition, we observe a small readout cross talk, i.e., a variation of up to 2% in the probability of an outcome of readout j depending on the state of the other qubit. All these effects are calibrated by measuring the four p_{uv} probabilities for each of the four $|uv\rangle$ states, which allows us to calculate a 4×4 readout matrix $\mathcal{R}$ linking the p_{uv}'s to the $|uv\rangle$ populations.

Repeating the pulse sequence shown in Fig. 1(c) at $M^I = 5.247$ GHz, $M^{II} = C = 5.125$ GHz, $R^I = 5.80$ GHz, $R^{II} = 5.75$ GHz, and applying the readout corrections $\mathcal{R}$, we observe the coherent exchange of a single excitation initially stored in qubit I. We show in Fig. 2 the time evolution of the measured $|uv\rangle$ populations, in fair agreement with a prediction obtained by integration of a

simple time independent Liouville master equation of the system, involving the independently measured relaxation times $T_1^I = 0.44$ μs and $T_1^{II} = 0.52$ μs, and two independent effective pure dephasing times $T_\varphi^I = T_\varphi^{II} = 2.0$ μs as fitting parameters. Tomographic reconstruction of the register density matrix ρ is obtained by measuring the expectation values of the 15 two-qubit Pauli operators $\{P_k\} = \{I, X, Y, Z\}_I \otimes \{I, X, Y, Z\}_{II} - \{II\}$, the X_j and Y_j measurements being obtained using tomographic pulses $\vec{Y}_j (-90°)$ or $\vec{X}_j (90°)$ just before readout. The ρ matrix is calculated from the Pauli set by global minimization of the Hilbert-Schmidt distance between the possibly nonphysical ρ and all physical (i.e., positive-semidefinite) ρ's. This can be done at regular intervals of the coupling time to produce a movie of $\rho(\Delta t)$ (see the Supplemental Material [14]) showing the swapping of the $|10\rangle$ and $|01\rangle$ populations at frequency $2g$, the corresponding oscillation of the coherences, as well as the relaxation towards $|00\rangle$. Figure 2 shows $\{\langle P_k \rangle\}$ and ρ only at $\Delta t = 0$ ns and after a $\sqrt{iSWAP}$ obtained at $\Delta t = 31$ ns with Θ_j^{-1} rotations of $\theta_I \simeq -65°$ and $\theta_{II} \simeq +60°$. The fidelity $F = \langle \psi_{id}|\rho|\psi_{id}\rangle$ of ρ with the ideal density matrices $|\psi_{id}\rangle\langle\psi_{id}|$ is 95% and 91%, respectively, and is limited by errors on the preparation pulse, statistical noise, and relaxation.

To quantify in a different way our ability to entangle the two qubits, we prepare a Bell state $|10\rangle + e^{i\psi}|01\rangle$ (with $\psi = \theta_{II} - \theta_I$) using the pulse sequence of Fig. 1(c) with $\Delta t = 31$ ns and no Θ_j^{-1} rotations, and measure the CHSH
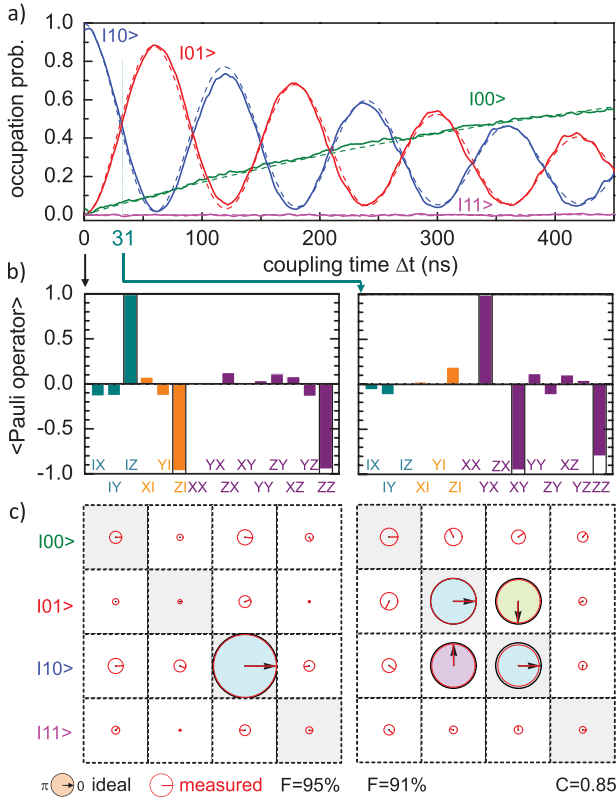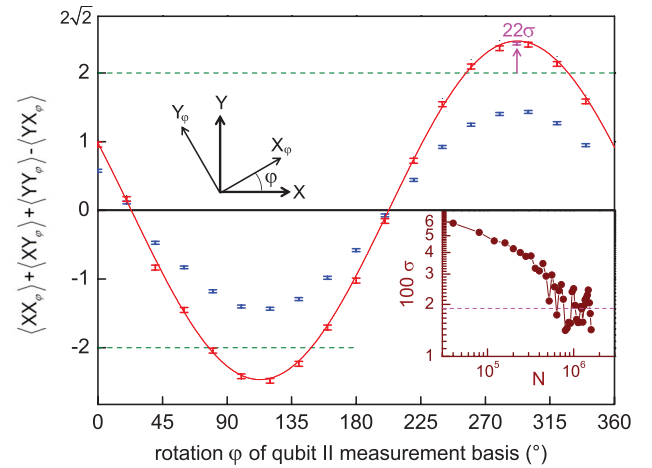

FIG. 2 (color). Coherent swapping of a single excitation between the qubits. (a) Experimental (solid lines) and fitted (dashed lines) occupation probabilities of the four computational states $|00\rangle \ldots |11\rangle$ as a function of the coupling duration. No Z or tomographic pulses are applied here. (b),(c) State tomography of the initial state (left) and of the state produced by the $\sqrt{iSWAP}$ gate (right). (b) Ideal (empty bars) and experimental (color filling) expected values of the 15 Pauli operators $IX, \ldots, ZZ$. (c) Corresponding ideal (color-filled black circles with black arrow) and experimental (red circle and arrow) density matrices, as well as fidelity F and concurrence C. Each complex matrix element is represented by a circle with an area proportional to its modulus (diameter equals cell size for unit modulus) and by an arrow giving its argument. See Sec. VI of the SM [14] for a real and imaginary part representation of the matrices.

FIG. 3 (color). Test of the CHSH-Bell inequality on a $|10\rangle + e^{i\psi}|01\rangle$ state by measuring the qubits along X^I or Y^I and X_φ^{II} or Y_φ^{II} (see top-left inset), respectively. Blue (red) error bars are the experimental CHSH entanglement witness determined from the raw (readout-error corrected) measurements as a function of the angle φ between the measuring basis, whereas solid line is a fit using ψ as the only fitting parameter. Height of error bars is ± 1 standard deviation $\sigma(N)$ (see bottom-right inset), with N the number of sequences per point. Note that averaging beyond $N = 10^6$ does not improve the violation because of a slow drift of φ.

entanglement witness $\langle XX_\varphi \rangle + \langle XY_\varphi \rangle + \langle YY_\varphi \rangle - \langle YX_\varphi \rangle$
as a function of the angle φ between the orthogonal
measurement bases of qubits I and II. Figure 3 compares
the results obtained with and without correcting the
readout errors with what is theoretically expected from
the decoherence parameters indicated previously:
unlike in [11] and because of a readout contrast limited
to 70%–75%, the witness does not exceed the classical
bound of 2 without correcting the readout errors. After
correction, it reaches 2.43, in good agreement with the
theoretical prediction (see also [16]), and exceeds the
classical bound by up to 22 standard deviations when
averaged over 10^6 sequences.

In a last experiment, we characterize the imperfections of
our $\sqrt{i\text{SWAP}}$ gate by quantum process tomography [1].
We build a completely positive map $\rho_{\text{out}} = \mathcal{E}(\rho_{\text{in}}) = \sum_{m,n} \chi_{mn} P'_m \rho_{\text{in}} P'^\dagger_n$ characterized by a 16×16 matrix χ
expressed here in the modified Pauli operator basis $\{P'_k\} = \{I, X, Y' = iY, Z\}^{\otimes 2}$, for which all matrices are real. For that
purpose, we apply the gate (using pulse sequences similar to
that of Fig. 1(c), with $\Delta t = 31$ ns and Θ_j^{-1} rotations) to the
16 input states $\{|0\rangle, |1\rangle, |0\rangle + |1\rangle, |0\rangle + i|1\rangle\}^{\otimes 2}$ and charac-
terize both the input and output states by quantum state
tomography. By operating as described previously, we
would obtain apparent input and output density matrices
including errors made in the state tomography itself, which
we do not want to include in the gate map. Instead, we fit the
16 experimental input Pauli sets by a model (see Sec. V of
the SM [14]) including amplitude and phase errors for the X
and Y preparation and tomographic pulses, in order to
determine which operator set $\{P^e_k\}$ is actually measured.
The input and output matrices $\rho_{\text{in,out}}$ corrected from the
tomographic errors only are calculated by inverting
the linear relation $\{\langle P^e_k \rangle = \text{Tr}(\rho P^e_k)\}$ and by applying it to
the experimental Pauli sets. We then calculate from the
$\{\rho_{\text{in,out}}\}$ set an Hermitian χ matrix that is not necessarily
physical due to statistical errors, and which we render
physical by taking the nearest Hermitian positive matrix.
This final χ matrix is shown and compared to the ideal
matrix χ_{id} in Fig. 4, which yields a gate fidelity $F_g = \text{Tr}(\chi\chi_{\text{id}}) = 0.9$ [17] for a single run of the gate. To better
understand the imperfections, we also show the map $\tilde{\chi}$ of
the actual process preceded by the inverse ideal process
[18]. The first diagonal element of $\tilde{\chi}$ is equal to F_g by
construction. Then, main visible errors arise from unitary
operations and reduce fidelity by 1%–2% (a fit yields a too
long coupling time inducing a 95° swap instead of 90° and
$\theta_{\text{I,II}}$ rotations too small by 3.5° and 7°, respectively). On the
other hand the known relaxation and dephasing times re-
duce fidelity by 8% but is barely visible in $\tilde{\chi}$ due to a spread
over many matrix elements with modulus of the order of or
below the 1%–2% noise level.

In conclusion, we have demonstrated a high fidelity
$\sqrt{i\text{SWAP}}$ gate in a two Josephson qubit circuit with individ-
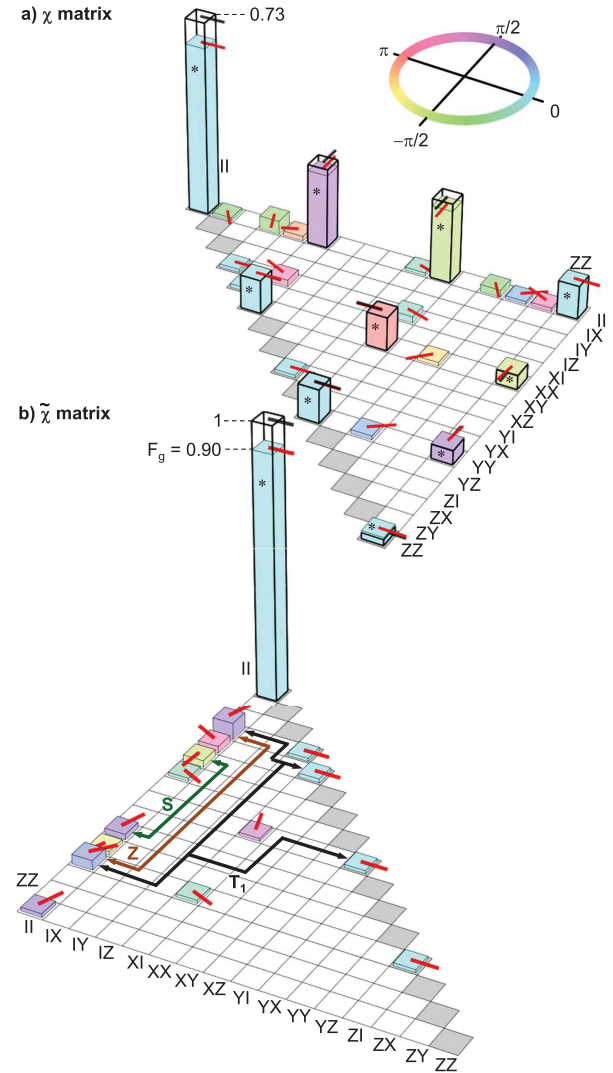ual nondestructive single-shot readouts, observed a

FIG. 4 (color). Map of the implemented $\sqrt{i\text{SWAP}}$ gate yielding
a fidelity $F_g = 90\%$. Superposition of the ideal (empty thick
bars) and experimental (color-filled bars) upper part of the
Hermitian process matrix χ (a) and lower part of the
Hermitian error matrix $\tilde{\chi}$ (b), in the two-qubit Pauli operators
basis $\{II, \ldots, ZZ\}$. Expected elements are marked with a star,
and elements below 1% are not shown. Each complex matrix
element is represented by a bar with height proportional to its
modulus and by an arrow at the top of the bar (as well as a filling
color for the experiment—see top inset) giving its argument. See
also Sec. VI of the SM [14] for a real and imaginary part
representation of these matrices and for additional information.
Labeled arrows indicate the main visible contributions to errors,
i.e., a too long swapping time (S), too small rotations $\theta_{\text{I,II}}$ (Z),
and relaxation (T_1)—see text.

violation of the CHSH-Bell inequality, and followed the
register's dynamics by tomography. Although quantum
coherence and readout fidelity are still limited in this circuit,
they are sufficient to test in the near future simple quantum
algorithms and get their result in a single run, which would
demonstrate the concept of quantum speed-up.

[1] M. A. Nielsen and I. L. Chuang, *Quantum Computation and Quantum Information* (Cambridge University Press, Cambridge, England, 2000).
[2] J. Clarke and F. Wilhelm, Nature (London) **453**, 1031 (2008).
[3] L. DiCarlo et al., Nature (London) **460**, 240 (2009).
[4] L. DiCarlo et al., Nature (London) **467**, 574 (2010).
[5] T. Yamamoto et al., Phys. Rev. B **82**, 184515 (2010).
[6] R. C. Bialczak et al., Nature Phys. **6**, 409 (2010).
[7] J. M. Chow et al., Phys. Rev. Lett. **107**, 080502 (2011).
[8] J. Koch et al., Phys. Rev. A **76**, 042319 (2007).
[9] J. A. Schreier et al., Phys. Rev. B **77**, 180502(R) (2008).
[10] M. Mariantoni et al., Science **334**, 61 (2011).
[11] M. Ansmann et al., Nature (London) **461**, 504 (2009).
[12] I. Siddiqi et al., Phys. Rev. Lett. **93**, 207002 (2004).
[13] F. Mallet et al., Nature Phys. **5**, 791 (2009).
[14] See Supplemental Material at http://link.aps.org/supplemental/10.1103/PhysRevLett.108.057002 for additional information about the sample preparation and experimental setup, the two-qubit Hamiltonian, the sample parameters, the readout characterization, the removal of errors on tomographic pulses, as well as for different representations of the matrices shown in Figs. 2 and 4.
[15] The relaxation times $T_1 \sim 0.5$ μs are twice as low as in Ref. [13], which is likely due to a lack of control of the electromagnetic impedance as seen from the qubit in the present and more complicated circuit and/or to the large asymmetry d of the transmons that opens a new relaxation channel.
[16] J. M. Chow et al., Phys. Rev. A **81**, 062325 (2010).
[17] Note that F_g is also equal to Shumacher's fidelity $\mathrm{Tr}[S_{\mathrm{id}}^{\dagger}S]/\mathrm{Tr}[S_{\mathrm{id}}^{\dagger}S_{\mathrm{id}}]$ with S (S_{id}) the super operator of the actual (ideal unitary) process and that fidelities F for the 16 output states range between 80% and 99.5%.
[18] A. G. Kofman and A. N. Korotkov, Phys. Rev. A **80**, 042103 (2009); private communication.